Pergamon

Int. J. Heat Mass Transfer. Vol. 39, No. 9, pp. 1815–1826, 1996
Copyright © 1996 Elsevier Science Ltd
Printed in Great Britain. All rights reserved
0017-9310/96 $15.00+0.00

0017-9310(95)00277-4

Convective heat transfer of rotating spheres and spheroids with non-uniform surface temperatures

GUOGUANG ZHENG and ROLAND LIST†

Department of Physics, University of Toronto, Toronto, Ontario M5S 1A7, Canada

(*Received* 29 *December* 1994 *and in final form* 21 *July* 1995)

Abstract—The latitudinal and overall convective heat transfer of rotating spheres and spheroids with axis ratios of $0.50 \leqslant \alpha \leqslant 1.0$ and limited thermal diffusivity and, thus, non-uniform surface temperatures was experimentally investigated in a wind tunnel over the range of Reynolds numbers $1.1 \times 10^4 < Re < 5.2 \times 10^4$. The surface temperature was remotely measured with an "AGEMA 800" thermal imaging system during particle cooling in the tunnel. A numerical technique was then used to calculate the time-evolution of the temperature distribution within the particle and the convective heat transfer coefficients at the surface. The results indicate how the convective heat transfer of rotating particles varies with latitude, the rotation rate (equivalent to Strouhal numbers $0 \leqslant Sr \leqslant 0.06$) and the position of rotation axis. Within experimental error, these factors do not influence the *total* heat transfer. However, they will be of importance in two-component, three-phase systems where deposition of substances, chemical reactions including release of latent heat, radiation and other processes are specific to site and local temperature. The present study, directed towards the local transfer rates controlling hailstone growth, provides the basic method of how to approach such complex situations. The overall Nusselt number, determined by integrating latitudinal heat transfer over the whole particle surface, was parameterized as a function of Reynolds number and axis ratio. Good agreement was found between this parameterization and direct overall measurements by other authors, indicating that thermal diffusivity changes from copper and aluminum to ice have a negligible effect.

INTRODUCTION

Most studies of convective heat transfer have been devoted to plates, cylinders and spheres with high thermal conductivities (Cu, Al, etc.) and virtually uniform surface temperature. Little effort has been directed towards the study of transfer processes for particles with more representative thermal conductivities and shapes, which are of particular interest in multi-phase and multi-component heat and mass transfer. In such cases additional processes dependent on surface location and temperature may also provide other heat sources through accretion of non-inert or non-equilibrium substances, phase changes, chemical reactions, radiation, etc. The range of study will be focusing on rotating spheroids with limited thermal conductivity and, thus, non-uniform surface temperature where convection–conduction is just one particular process. The applied method can then be easily extended to more complex situations.

Understanding of the transfer from spheroids is important in the study of hail growth since the most commonly observed large hailstones with diameters between 2 and 5 cm (corresponding to Reynolds numbers of 10^4–10^5) can be approximated by oblate spheroids [1–5]. The heat transfer is essential because the hail growth rate is controlled by the location and rate of accretion of cloud droplets, their heat content relative to the local surface temperature, and the latent heat of freezing, produced by freezing of the accreted droplets.

Freely falling hailstones were found to be tumbling [6], which can be described by a rotation of gyration mode superimposed to free fall [1, 2, 7]. These motions have a rotational symmetry. Thus, 'local' means 'latitudinal'. The latitudinal transfer coefficient is a key factor in determining local hailstone growth. To disentangle the complexities of non-uniform local transfer from those averaged over the whole surface, the latitudinal processes have to be investigated at a resolution sufficient to address local growth and any other multi-component and multi-phase processes.

In the previous theories on heat and mass transfer, hailstones were treated as spherical particles with uniform temperatures over the whole surface [8–10]. Macklin [2] was the first to make measurements of the melting rate of fixed spheroidal ice particles in an airflow and found more mass and heat transferred from spheroids than from spherical particles with the same major diameter. He introduced a shape factor as did List and Dussault [11]. The Nusselt number, Nu, used in their applications, was based on extrapolations of expression by Ranz and Marshall [12] who measured the evaporation of freely falling liquid

† Author to whom correspondence should be addressed.

NOMENCLATURE

A	surface area of the particle [m^2]
C	constant in equation (8)
c_p	specific heat of solid (ice and MGC) [J kg^{-1} K^{-1}]
D	major axis diameter/characteristic length of the particle [m]
f_1	rotaton rate [Hz]
k_a	thermal conductivity of air [W m^{-1} K^{-1}]
k_i	thermal conductivity of solid (ice and MGC) [W m^{-1} K^{-1}]
m	power factor of Reynolds number in equation (8)
n	power factor of Prandtl number in equation (8)
Nu, Nu_ϕ	local and latitude-dependent Nusselt number, respectively
$\overline{Nu}$	overall or macroscopic Nusselt number
Pr	Prandtl number
$\dot{q}_{s,CC}$	heat flux from the surface by convection and conduction [J m^{-2} s^{-1}]
$\dot{q}_{s,CON}$	conductive heat flux normal to the surface [J m^{-2} s^{-1}]
$\dot{q}_{s,ESD}$	heat flux normal to the surface by evaporation, sublimation/deposition [J m^{-2} s^{-1}]
$\dot{q}_{s,R}$	heat flux from the surface by radiation [J m^{-2} s^{-1}]
r	distance from the particle center (defined in Fig. 3) [m]
Re	Reynolds number (based on the major axis diameter (D) of the particle)
Re^*	Reynolds number defined by Skelland and Cornish [13]
Sc	Schmidt number
Sh	Sherwood number
Sr	Strouhal number
t	time [s]
T	temperature within the particle [K]
T_a	air temperature [K]
T_i	initial particle temperature [K]
T_s	particle surface temperature [K]
V_a	air speed [m s^{-1}]
z	distance from the equatorial plane [m].

Greek symbols

α	axis ratio, i.e. ratio of the minor to major axis of spheroid
α_i	thermal diffusivity of solid (ice and MGC) [m^2 s^{-1}]
χ	ratio of heat transfer from a spheroid to that of a sphere with the same diameter
ϕ	latitude (defined in Fig. 3)
ρ_i	solid (ice and MGC) density [kg m^{-3}]
ϑ	azimuthal angle (defined in Fig. 3).

Subscripts

a	air
i	solid (ice and MGC); initial value
s	surface of the particle
ϕ	latitude.

drops for Reynolds number $0 \leqslant Re \leqslant 200$. Skelland and Cornish [13] determined Nu of fixed, solid and oblate spheroids with axis rations of 0.33–1.0 over $120 < Re < 6000$. They also found that shape is important for the transfer rates. A numerical investigation on the heat and mass transfer of spheroids in steady axisymmetric flow ($1 \leqslant Re \leqslant 100$) was reported by Masiliyah and Epstein [14], which illustrated the latitude-dependence of Nu. Unfortunately, very few experiments have been addressing the heat transfer from spheroids over the (relatively high) range of Reynolds numbers applicable to hailstones [15]. Further, experimental work on the heat transfer of spinning particles was limited because of the difficulty in measuring directly the surface and/or internal temperatures. Thus, extensive experiments were necessary by applying modern experimental and numerical techniques to investigate the local heat transfer from spheroids with different axis ratios and under different rotation modes. This was achieved by remote measurement of the surface temperature distributions of particles cooling in an airflow and numerical calculation of the internal temperature distributions and, then, the local heat flux at the surface.

EXPERIMENT

Wind tunnel system

The present experimental study on heat transfer of rotating spheroids was carried out in the University of Toronto Cloud Physics Wind Tunnel. It has a vertical closed circuit (Fig. 1) and its temperature, velocity, pressure, liquid water content and particle rotational motions can be controlled. Thus, natural cloud conditions and aerodynamic motions of hailstones can be simulated. The tunnel is composed of square and rectangular aluminum ducts. From Fig. 1 it can be observed that a 3.7 kW motor (1) drives a centrifugal fan (2) which takes in horizontally moving air and propels it downwards (3). Turning vanes (5 and 9) divert the airflow through the cooling elements (7) and upwards into a contraction (11), which funnels

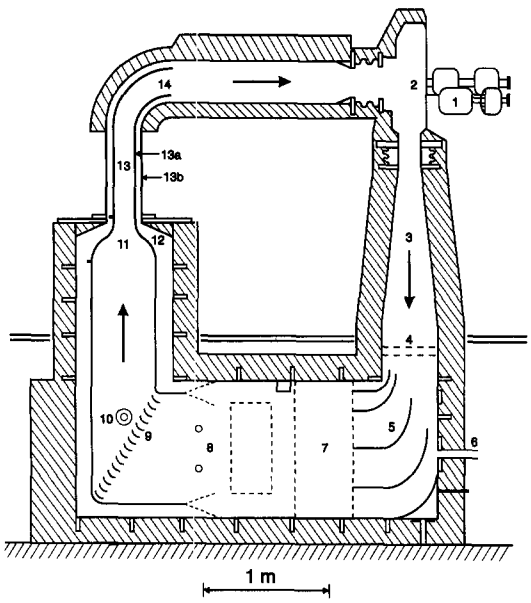

Fig. 1. Vertical cross-section of the University of Toronto Cloud Physics Wind Tunnel with (1) motor, (2) fan, (3) airflow, (4) heaters, (5) turning vanes, (6) pressure values, (7) cooling elements, (8) double wall flaps, (9) turning vanes, (10) water injection system, (11) contraction, (12) outer duct, (13) measuring section (a, inner wall and b, outer wall) and (14) return duct; airflow in the direction of arrows.

the airflow into the measuring section (13). The air is then returned through a duct (14) to the fan. A complete description of the tunnel and its performance can be found in [7].

The experiments were carried out in the measuring section (schematic diagram, Fig. 2). This unit is 70 cm high, and has a cross-section of 17.8 cm × 17.8 cm and a double wall, with the inner enclosing the experimental region and insulating it from the temperature gradient within the outer square 'ring'. The outer walls consist of four aluminum plates which are used as the mounting platforms for the particle suspension system, an infrared scanner, camera and a door to access to the inner duct. To measure the surface temperature of the test particles at different angles, the scanner and door plates were interchanged during repeat runs to allow measurements in orthogonal positions. The air velocity was varied between 6.6 and 30 m s^{-1} and held within ± 0.2 m s^{-1}. Measurements with a hot wire anemometer across the central 10 cm × 10 cm showed that the velocity profile was constant within 5%, while the turbulence (root mean square of the velocity fluctuation) was less than 0.5% [15]. The ambient air temperature could be controlled between 0°C and −30°C within ±0.2°C.

The particle-suspension system was used to rotate the test model at rates between 0 and 50 Hz in the airflow, with its minor axis normal to the airflow. The horizontal rotation axis pointed into the measuring section at an angle of 30° to the axis of the rotator plate [see Fig. 2 and 3(a)]. This also allows simultaneous measurements of equatorial and polar surface temperatures. Another device allowed a vertical rotation parallel to the airflow [Fig. 3(b)].

The test particles

The experiments were motivated by the need to understand the heat transfer of ideal spherical and spheroidal hailstones. Thus, smooth models were created using materials with thermal properties similar to those of hailstones. Obviously, bulk ice ($\rho_i = 915$ kg m^{-3}) is best. However, in order to investigate pure convective heat transfer without sublimation and evaporation, some models, polished to a smooth finish, were made of Machinable Glass Ceramic (MGC), which has thermal properties similar to those of ice ($\alpha_{MGC} = 0.81$ m^2 s^{-1} and $\alpha_{ICE} = 1.16$ m^2 s^{-1}) [16]. A polyvinyl chloride (PVC) dowel, 3.2 mm in diameter and 65.0 mm in length, was glued into the model for support during the superimposed rotational motions. The ice models with major axis diameter of 2 and 3 cm and aspect ratios of 0.5, 0.67 and 1.0 were produced by freezing distilled water in smooth rubber molds at a temperature of −20°C.

Surface temperature measurements

An "AGEMA Infrared System Thermovision 800" thermal imaging system was used to remotely scan the surface temperature of the models (Fig. 2). The AGEMA detector consists of a mercury cadmium cell and has a spectral response over a 8–12 μm window with a sensitivity of ±0.13°C at −15°C. The system scanner has a 12° germanium interchangeable lens. With a 32 mm extension tube the lens has a working distance of 17 cm. The spot size at the particle surface was 2.0±0.5 mm. The scanning speed was 28 frames s^{-1}. About 400 points per cm^2 of the model surface could be resolved, i.e. enough to analyze the local heat transfer in detail. Calculations of the penetration depth of infrared radiation in ice indicated that 98% of the incident radiation is absorbed within the first 40 μm [17]. This means that the temperatures measured by the AGEMA system are representative of values very close to the model surface. The emissivity of ice and MGC was measured and showed no major change over a viewing angle between 0 and 60°, however, a sharp drop off occurred at angles >70° [16].

Experimental set-up

The experimental conditions were chosen to represent the environment of natural hailstones in terms of (1) air speed, varying between 6.6 and 24 m s^{-1} and approximating the terminal velocities of hailstones with diameters of 0.5–3 cm (corresponding to Reynolds numbers $1.1 \times 10^4 \leqslant Re \leqslant 5.2 \times 10^4$) and (2) air temperature, which was set at −15, −19 or −21°C and monitored with thermocouples to within ±0.2°C. The initial uniform temperature of the test particles was −6°C. The forced rotation rates were set between

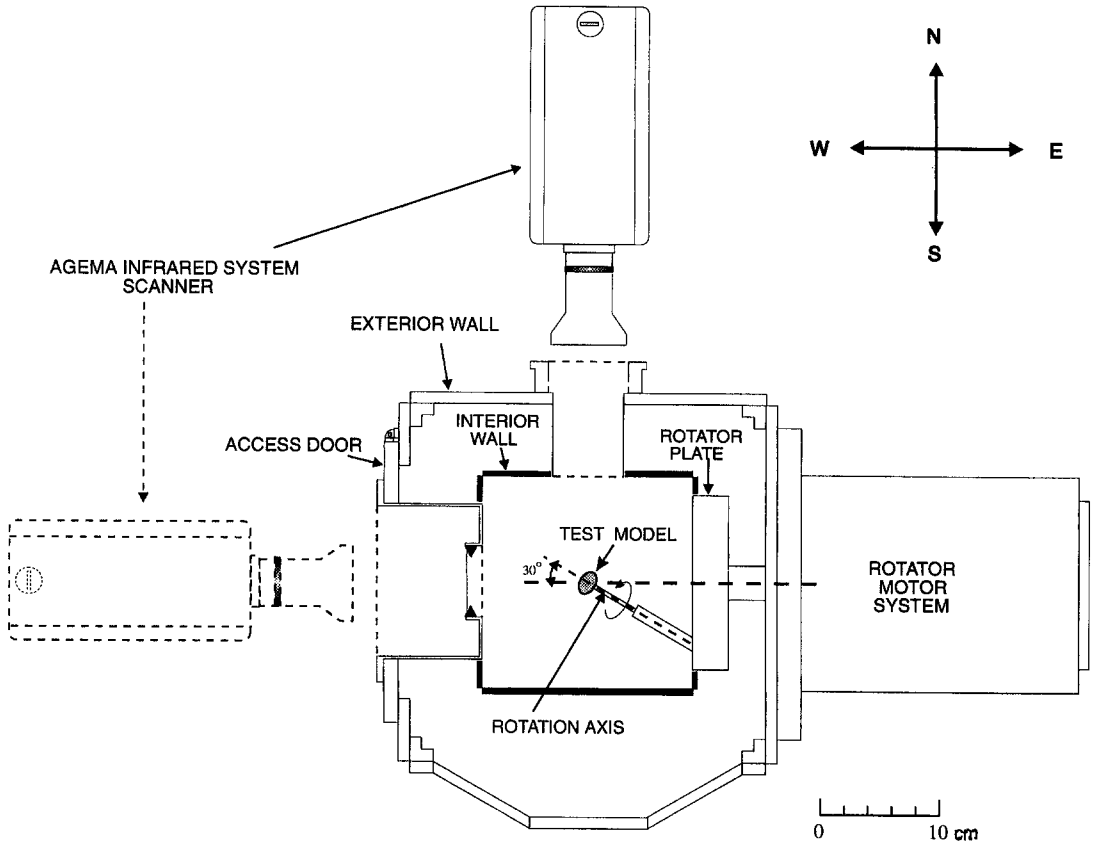

Fig. 2. Horizontal cross-section of the measuring section of the wind tunnel. The access door plate and the (AGEMA Infrared System) scanner system plate were interchangeable for repeat runs of experiments.

0 and 22 Hz. All experiments were performed at laboratory pressure (~ 102 kPa).

After the AGEMA system was calibrated, the model was transported to the wind tunnel and mounted on the rotator system. As the model was exposed to the airflow, the rotator was started and the experiment began. The AGEMA system continuously monitored and stored the evolving surface temperature distribution. Each experiment was performed at least twice to check for consistency and to view the model from two orthogonal directions (Fig. 2).

NUMERICAL CALCULATION

The temperature field within a particle

When a warm particle is exposed to a colder airflow, a temperature gradient develops in the particle and heat is conducted to the surface. The thermal diffusion or transient heat conduction equation [18, 19] is used to calculate the evolving temperature field $T(r,t)$ within the particle

$$\rho_i c_p \frac{\partial T(r,t)}{\partial t} = \nabla \cdot [k_i \nabla T(r,t)] \qquad (1)$$

where ρ_i is the density, c_p the specific heat of the particle and k_i the thermal conductivity. k_i can be assumed constant within the (small) range of temperature of the present experiments. Equation (1) is parabolic overall and elliptic in its spatial coordinates. The temperature field can be solved for finite time steps, starting with known initial and boundary conditions. The cylindrical polar coordinates (r, ϑ, z) (Fig. 3) were chosen to solve the internal temperature field

$$\frac{\partial T}{\partial t} = \alpha_i \left[\frac{\partial^2 T}{\partial r^2} + \frac{1}{r}\frac{\partial T}{\partial r} + \frac{\partial^2 T}{\partial z^2} + \frac{1}{r^2}\frac{\partial^2 T}{\partial \vartheta^2} \right] \qquad (2)$$

where $\alpha_i = k_i/(\rho_i c_p)$ is the thermal diffusivity, which is associated with the speed of propagation of heat within the particle. r represents the distance from the particle centre, ϑ the azimuth angle and z the distance from the equatorial or x–y plane. The rotational symmetry of surface temperature and internal temperature distribution about the minor axis causes $\partial^2 T/\partial \vartheta^2$ to vanish so that equation (2) reduces to two dimensions [16, 20, 21]. Since the temperature field at any time is not affected by the field at a later time, the calculation can be started with a given initial internal field and the measured surface temperature field, and stepped forward in time. Taking the temperatures calculated at time $t = 1$ as approximations for the unknown temperatures at time $t = 2$, and using the

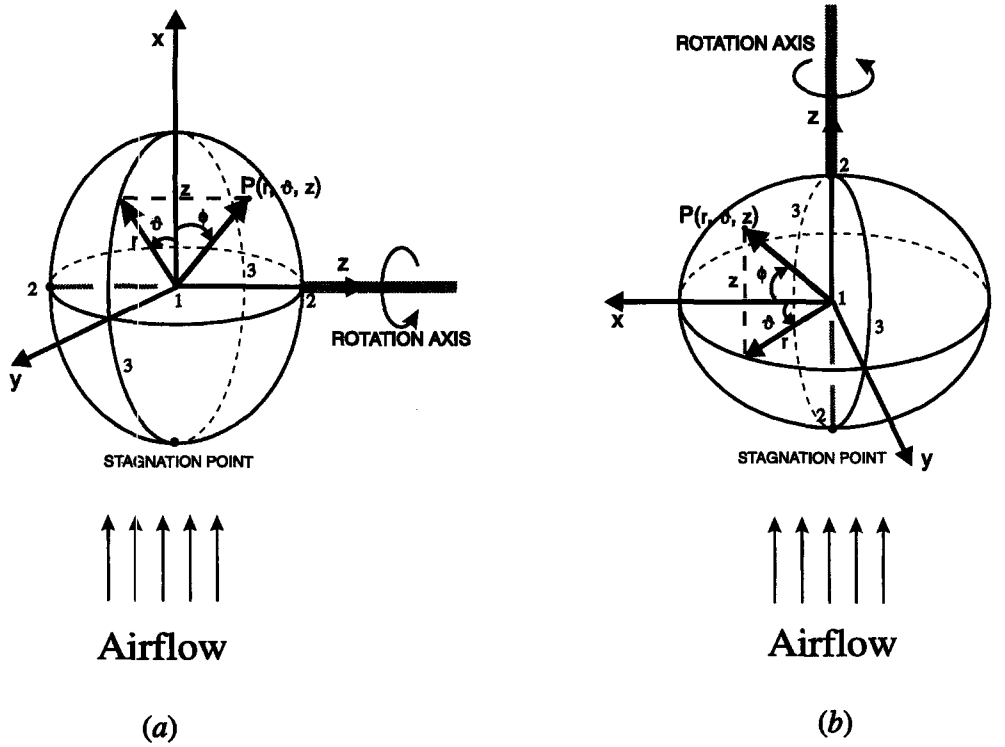

Fig. 3. Configuration of rotational axis and suspension stem of hailstone models, with cylindrical polar coordinates (r, ϑ, z); 1, hailstone center; 2, poles; 3, equator; ϕ, latitude, and ϑ, longitude; (a) rotational axis perpendicular to (vertical) airflow; (b) rotational axis parallel to airflow.

values of the surface temperature measurements (boundary conditions) at $t = 2$, the calculations are repeated until a solution of prescribed accuracy is achieved. Since the surface temperatures of the particle decrease steadily during cooling in the airflow, the solutions always converge. The same procedure is repeated to calculate the temperatures at the following time step.

In these calculations, a grid spacing (Δr and Δz) of 1 mm with a time step of 1 s gave good accuracy. Reducing the time step to 0.25 s gave identical results, while doubling the time step or grid spacing decreased the accuracy by 2–3%. The accuracy of the numerical calculation was also evaluated by comparing the numerical solution and the measurements with a thermocouple at the centre of a smooth non-rotating sphere cooling in an airflow as function of cooling time. It showed a very small temperature difference (<0.17°C) between the numerical values and the measurements [16]. This gives some indication of the consistency of the numerical solution.

The heat transfer coefficient

In the present work the convective heat transfer between a moving fluid and the surface of a solid particle is of special interest. For a cooling particle without any accretion of cloud droplets and their freezing, the rate of transfer at the surface into the surroundings must balance with the conduction from the interior. The energy balance equation is expressed by

$$\dot{q}_{s,CON} = \dot{q}_{s,CC} + \dot{q}_{s,ESD} + \dot{q}_{s,R} \tag{3}$$

where the subscript s stands for the surface. $\dot{q}_{s,ESD}$ and $\dot{q}_{s,R}$ represent the heat fluxes by phase changes through evaporation, sublimation or deposition and by thermal radiation, respectively. They are small ($<3\%$ and 5%, respectively) within the temperature range and conditions of the present experiments, and are neglected. Thus, the conductive heat flux normal to the surface within the particle, $\dot{q}_{s,CON}$, is in balance with the heat transfer rate by convection and conduction to the air, $\dot{q}_{s,CC}$, that is,

$$\dot{q}_{s,CON} = -k_i\left(\frac{\partial T}{\partial n}\right)_s = -\frac{k_a Nu}{D}(T_s - T_a) = \dot{q}_{s,CC} \tag{4}$$

where D is the major axis diameter of the particle, k_a the thermal conductivity of the fluid (air), $(\partial T/\partial n)_s$ the temperature gradient at the surface within the particle, and T_s and T_a are the temperatures of the particle surface and the ambient air, respectively. The Nusselt number, Nu, represents the dimensionless convective heat transfer coefficient which is equal to the dimensionless temperature gradient at the surface.

The local Nusselt number, Nu_j, at any surface element j can be written as

$$Nu_j = \frac{k_i D}{k_a(T_{sj} - T_a)} \left(\frac{\partial T}{\partial n}\right)_j. \quad (5)$$

For a given particle in a known environment, k_i, k_a, D and T_a are constants. T_{sj} can be measured as a function of time with the AGEMA system while $(\partial T/\partial n)_j$ is determined by solving the heat conduction equation (2). Once established, Nu_j can be obtained by equation (5).

In the present work, Nu_j in (5) is described as latitude-dependent because of the rotational symmetry. The overall or macroscopic Nusselt number, $\overline{Nu}$, is defined by two different but interlinked expressions

$$\overline{Nu} = \frac{\int_0^\pi Nu_\phi A(\phi)\,d\phi}{\int_0^\pi A(\phi)\,d\phi} = \frac{1}{A_s}\int_0^\pi Nu_\phi A(\phi)\,d\phi \quad (6)$$

and

$$\overline{Nu} = \frac{k_i D}{k_a(\bar{T}_s - T_a)} \overline{\left(\frac{\partial T}{\partial n}\right)_s} \quad (7)$$

where Nu_ϕ is the latitudinal Nusselt number over the surface area $A(\phi)$ between latitude ϕ and $\phi + d\phi$, and A_s the total surface area of the particle. $\bar{T}_s$ and $\overline{(\partial T/\partial n)_s}$ are determined by integrating over the area-weighted latitudinal temperatures and temperature gradients, respectively. Calculation shows that expression (7) yields a $\overline{Nu}$ approximately 5–10% smaller than that obtained by expression (6). In the present work $\overline{Nu}$ is determined by (6) because the averaging is physically more reasonable. $\overline{Nu}$ is often expressed in an exponential function of Reynolds and Prandtl numbers

$$\overline{Nu} = C\,Pr^n\,Re^m \quad (8)$$

where n, C and m are constants. A commonly adopted value of n is 1/3 [22, 23], with $Pr = 0.71$, within the relevant range of air temperatures and pressures for hail growth. The characteristic dimension for Re is the major axis diameter of the particle. A term "2.0", which is often added to the right-hand side of (8), representing the lower limit of heat transfer by molecular processes alone, is neglected here since it is small compared to the value of $\overline{Nu}$.

RESULTS AND DISCUSSION

Figure 4 gives an example of the surface temperature measurements, as established with the AGEMA system, of a 2 cm diameter spheroidal MGC particle, rotating about the minor axis perpendicular

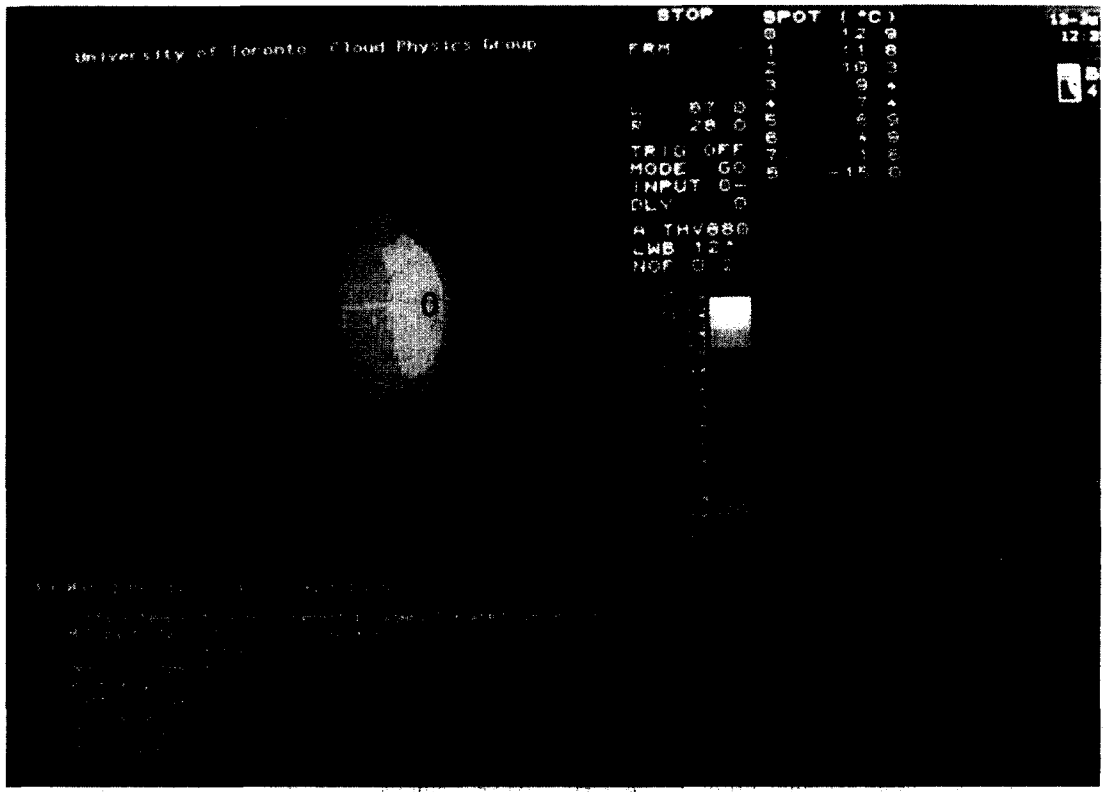

Fig. 4. Photograph of the infrared image on AGEMA monitor of a MGC particle cooling in the wind tunnel. The view of the particle surface is perpendicular to the 60° latitude and includes the pole (0) and part of the equator (5).

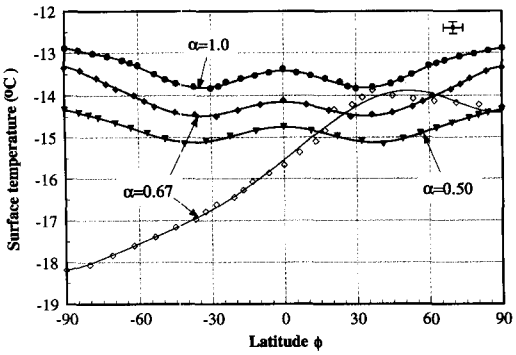

Fig. 5. Measured surface temperatures of rotating spheroidal ice particles ($D = 2$ cm, $T_i = -6°C$, $f_1 = 10$ Hz) with axial ratios of 0.5, 0.67 and 1.0, as function of latitude ϕ, 30 s after exposure to cold air flow ($T_a = -21°C$, $V_a = 15$ m s^{-1}, $Re = 2.5 \times 10^4$); configuration according to Fig. 3(a): thick line; thin line with hollow points for particles with minor axis parallel to airflow [configuration Fig. 3(b)].

to the airflow [configuration Fig. 3(a)]. The surface scan was taken 17 s after exposure to the cold airflow and shows that the surface temperature is a function of latitude ϕ. Figure 5 shows the measured surface temperatures of ice particles ($D = 2$ cm, $T_i = -6°C$) with axial ratios α of 0.5, 0.67 and 1.0, rotating at $f_1 = 10$ Hz about the minor axis perpendicular to (thick lines) [configuration Fig. 3(a)] and parallel to (thin lines) the airflow [configuration Fig. 3(b)], with $T_a = -21°C$, $V_a = 15$ m s^{-1}, $Re = 2.5 \times 10^4$, as function of latitude ϕ, at 30 s after exposure to the airflow. For the particles with the minor axis perpendicular to the airflow, the T_s–ϕ relation is wavelike and symmetric about $\phi = 0°$. This is caused by the configuration of rotation. To enhance this point and based on the symmetry of exposure, a negligible effect of the supporting stem [16] and some measurements at $\phi > 0°$, the measurements over $0° > \phi > -90°$ were also "flipped" to $90° > \phi > 0°$.

The surface temperature in the polar regions ($|\phi| \sim 90°$) is higher than that in the equatorial region ($\phi \sim 0°$), while the lowest temperature occurs near $|\phi| \sim 40°$. It is also seen in Fig. 5 that the more elliptical the particle is, the lower its heat content is and the lower the surface temperature becomes within a fixed time period. The latitude with the lowest surface temperature is shifted from $|\phi| = 30°$ to 40° as α decreases from 1.0 to 0.5. For the particle with the minor axis parallel to the airflow, the surface temperature is asymmetric and shows a large dependence on ϕ. The difference between the extreme temperatures at any given time is much larger than for the particle rotating about the minor axis perpendicular to the airflow. The lowest temperatures occur at the stagnation point ($\phi = -90°$), while the highest temperatures are found for ϕ between 30° and 60°. At 30 s after exposure to the airflow the maximum difference of the surface temperatures between the polar and equatorial regions is 0.8°C and 2.4°C for the particles with the vertical and horizontal rotation axes, respectively. These values are even larger at 10–20 s after exposure (not shown here).

The internal temperature of a cooling particle is numerically calculated from the transient heat conduction equation (2) by using the measurements of the time-variation of surface temperature. Two examples are given for the cross-section through the minor axis of an ice particle rotating about the horizontal [configuration Fig. 3(a)] and vertical axes [Fig. 3(b)] in Figs. 6(a) and (b), respectively. They were taken 20 s after exposure to the airflow. Since the particle was initially warmer than the ambient air, the internal temperature always decreased outwards. It can be seen from Fig. 6(a) that there is a symmetry about the centre with the hottest region for the particle rotating about the minor axis perpendicular to the airflow. In the case of the minor axis parallel to the airflow, the symmetry about the equatorial plane is not maintained and the hottest point is on the minor axis roughly two-thirds of the distance from the front to the rear stagnation points [see Fig. 6(b)]. It can also be seen from the time-evolution of the internal temperature (Fig. 7) that the hottest point is gradually shifted from the centre to the rear part of the particle and the temperature gradient becomes small with time. It was further established that the latitudinal Nusselt number remained constant with time as the cooling progressed. However, the highest accuracies can be achieved in the presence of large temperature gradients, i.e. close to the beginning of the individual experiments when possible initial unevenness has died down.

The latitude-dependent Nusselt number, Nu_ϕ, for particles with $\alpha = 0.5$, 0.67 and 1.0, rotating at $f_1 = 10$ Hz, is shown in Fig. 8. As expected, low Nu_ϕ reflects the high surface temperatures of Fig. 5, thus, repeating the wave-like behavior, but with a 90° shift in latitude. The calculations show that ice particles produce Nu_ϕ similar to MGC ones with the same shape, although the surface temperature of the former is somewhat lower than that of the latter [16] because of the 30% difference in thermal conductivities. This experimental/numerical finding also gives confidence into the applied methods and the neglect of radiation and evaporation processes. Starting at $\phi = -90°$, Nu_ϕ for the particles with the minor axis perpendicular to the airflow increases with increasing ϕ. A maximum value is reached at ϕ between −45° and −35°. Then, Nu_ϕ decreases with ϕ and a minimum is reached at $\phi = 0°$. For the particles with the minor axis parallel to the airflow, Nu_ϕ in the forward region ($\phi < 0°$) is significantly higher than that in the rear part ($\phi > 0°$). Starting at the front stagnation point ($\phi = -90°$), Nu_ϕ changes little with ϕ, and then decreases with increasing ϕ. There is a sharp fall of Nu_ϕ at ϕ between −30° and 5°, and the minimum can be associated with the separation point (at ϕ between 0° and 10°) of the flow. Then, Nu_ϕ increases with ϕ. Nu_ϕ is also dependent on α, and the less α is, the higher Nu_ϕ becomes. The latitudinal variation of Nu_ϕ also increases as α

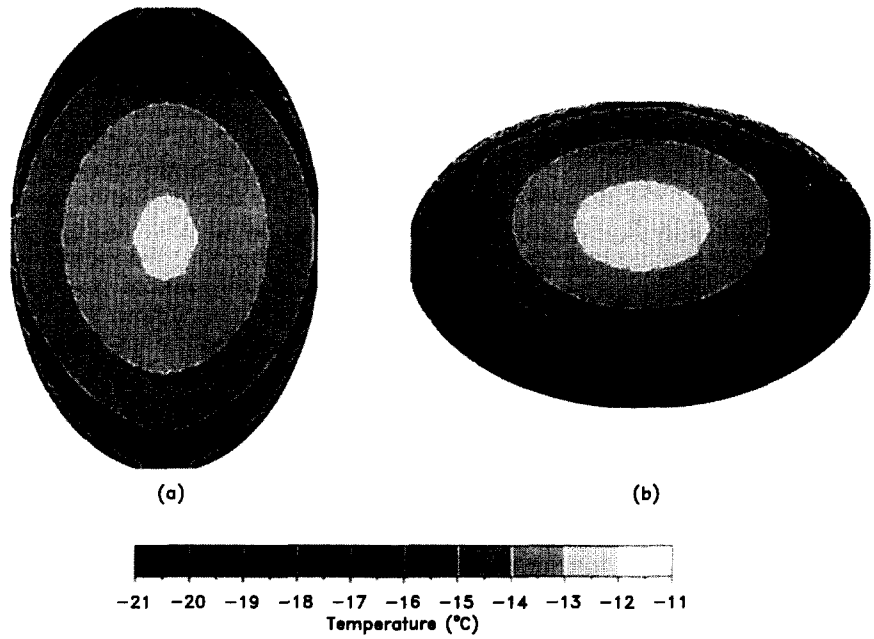

Fig. 6. The internal temperature distribution of an ice spheroid ($D = 2$ cm, $\alpha = 0.67$, $T_i - 6°C$), cooling in an airflow ($T_a = -21°C$, $V_a = 15$ m s^{-1}, $Re = 2.5 \times 10^4$), with the minor axis perpendicular to [a, configuration Fig. 3(a)] and parallel to the airflow [b, configuration Fig. 3(b)], at 20 s after exposure to the airflow.

decreases. Although a similarity in the Nu_ϕ distribution exists for particles with different α, Nu_ϕ for a spheroidal particle is higher than that for a spherical particle with the same diameter. The latitudinal variation of Nu_ϕ reaches 25–45% of its latitude-average value for rotating particles with the minor axis perpendicular to the airflow and over 100% for the particles with the minor axis parallel to the airflow. This demonstrates the non-uniform and latitudinal character of the heat transfer.

For many applications, only overall transfers are represented by $\overline{Nu}$ are of importance. Figure 9 gives $\overline{Nu}$ of the particles in the configuration of Fig. 3(a), rotating at $f_1 = 10$ Hz, with $\alpha = 0.5$, 0.67 and 1.0, as a function of Re. It is apparent that $\overline{Nu}$ increases with increasing Re and can be fitted to (8). It has been customary to assume that the power factor of Re in (8) is 1/2 [22, 23]. However, this assumption is only valid when a laminar boundary layer exists. At higher Re, the main contributions to the heat transfer are from the laminar front region and from the turbulent wake region of the particles. Rotation causes any given point on the particle surface to move from the forward region to the rear section and back to the front. Thus, the heat transfer process becomes more complicated than that in a simple laminar boundary layer. It could be described by 'mixing' of laminar and turbulent flows around the particle. The occurrence of a turbulent boundary layer could increase the heat transfer from the particle to the fluid at a rate greater than $Re^{1/2}$, and that its effect becomes increasingly more important as Re increases (Fig. 9). As shown in Fig. 9, the $Re^{1/2}$ power law is not a good fit for the experimental results of rotating particles in the Re range of this study. It can also be expected that the shape of the particle, i.e. α, would influence the flow around it and hence, the heat transfer to air. Indeed, spheroids can produce $\overline{Nu}$ up to 40% larger than for spheres with the same diameter. Further, spheroidal particles have a surface area larger than that of a sphere with the same volume and, therefore, a larger heat loss. The investigations by Macklin [2] for non-rotating, melting ice spheroids made this point. As shown in Fig. 9, the relationship between $\overline{Nu}$ and Re can be fitted to (8) by

$$\overline{Nu} = (0.236 + 0.094\alpha) Re^{(0.0658 - 0.088\alpha)} \quad (9)$$

with the correlation coefficient of $\log(\overline{Nu})$ vs $\log(Re)$ being 0.983. The power factor of Re is $> 1/2$ and increases with decreasing α. For a spherical particle with $\alpha = 1.0$, $m = 0.57$.

Alternately, a linear approximation can also be used to represent $\overline{Nu}(Re)$ as shown in Fig. 9 (thin lines).

$$\overline{Nu} = (55.6 - 13.5\alpha) + (0.00458 - 0.00218\alpha) \times 10^{-4} Re. \quad (10)$$

It is apparent that the experimental data can be fitted, within experimental error, by a straight line or with a power law. The exponential version (9) is given because such an approximation is expected whereas the linear approximation (10) is simpler to use. Both equations (9) and (10) and the related conclusions are considered valid within the Re range of the experiments ($1.1 \times 10^4 \leqslant Re \leqslant 5.2 \times 10^4$).

It might be expected that rotation could induce a

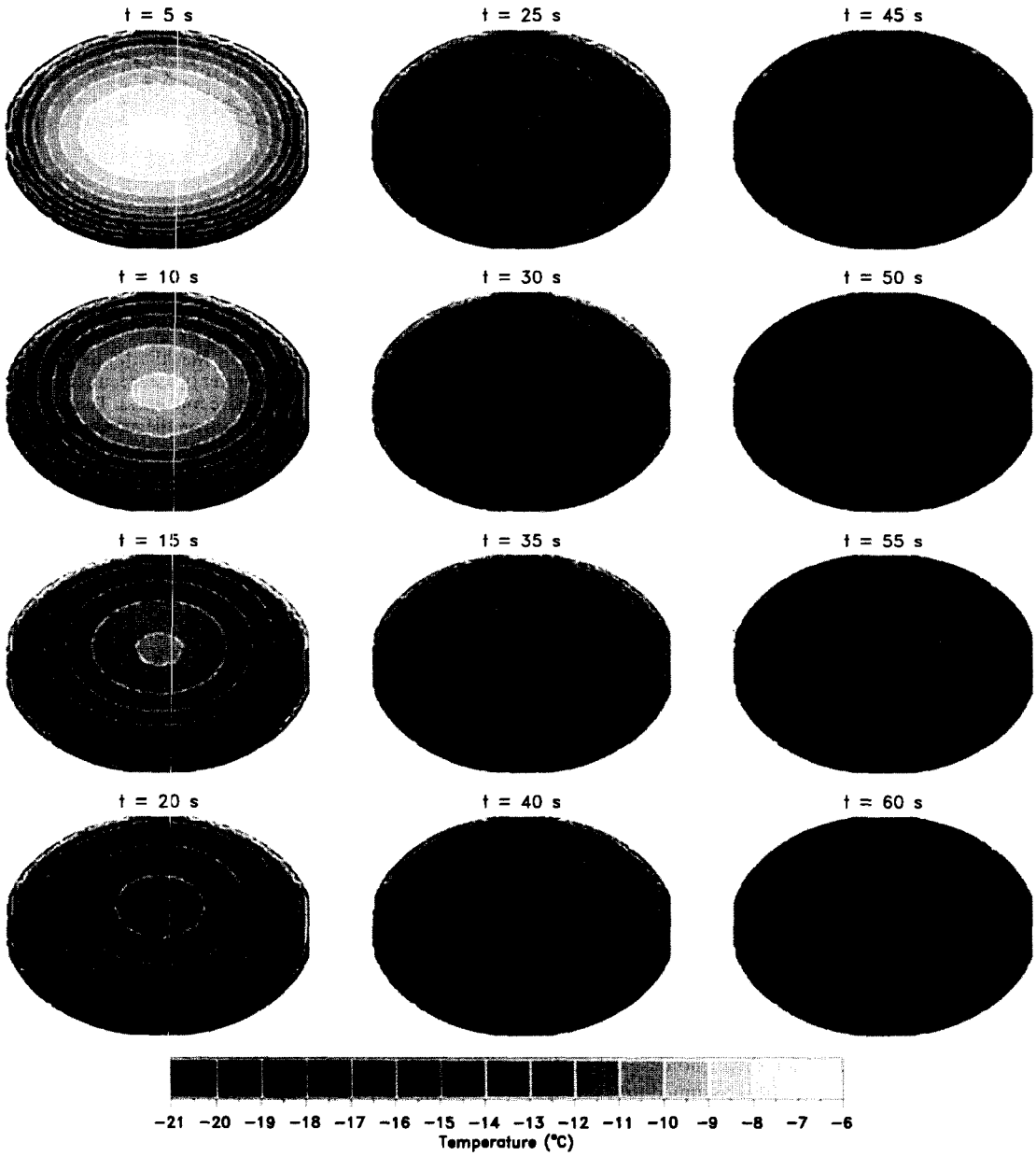

Fig. 7. The time-evolution of the internal temperature distribution of an ice spheroid ($D = 2$ cm, $\alpha = 0.67$, $T_i = -6°C$), cooling in an airflow ($T_a = -21°C$, $V_a = 15$ m s^{-1}, $Re = 2.5 \times 10^4$), with the minor parallel to the airflow [configuration Fig. 3(b)].

secondary flow around the particle, with consequences for the convective heat transfer. However, this has not been detected in the present investigation because the rotation rates of $5 \leqslant f_1 \leqslant 22$ Hz reflect only low Strouhal numbers ($Sr = f_1 D/V_a$) of $0.005 < Sr < 0.06$, which do not significantly influence the flow field around the particle. Further, the variation of Nu_ϕ for the particles with the minor axis parallel to the airflow is four to five times higher than for the case perpendicular to the airflow (Fig. 8). However, $\overline{Nu}$ is only 5–10% higher [16] (not shown here), which is within the error bar of the measurements. This indicates that the position of the rotation axis has little effect on the total convective heat transfer.

COMPARISON OF $\overline{Nu}$ WITH OTHER INVESTIGATIONS

No data could be found in the literature on the local (latitudinal) Nusselt number of rotating particles and very few experimental studies have been directed towards the heat transfer from spheroids over the range of relative high Reynolds numbers. Thus, this comparison will be restricted to overall transfer of

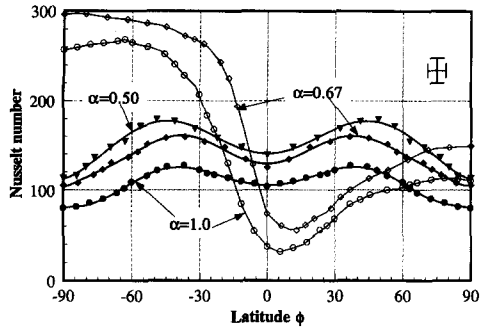

Fig. 8. The latitude-dependent Nusselt number, Nu_ϕ of ice particles ($D = 2$ cm, $T_i = -6°C, f_1 = 10$ Hz), rotating about an axis perpendicular to airflow ($T_a = -21°C$, $V_a = 15$ m s^{-1}, $Re = 2.5 \times 10^4$), with axial ratios of 0.5, 0.67 and 1.0, as function of latitude ϕ, 30 s after exposure to airflow [configuration Fig. 3(a)]; thin lines with hollow points for particles with minor axis parallel to the flow [Fig. 3(b)].

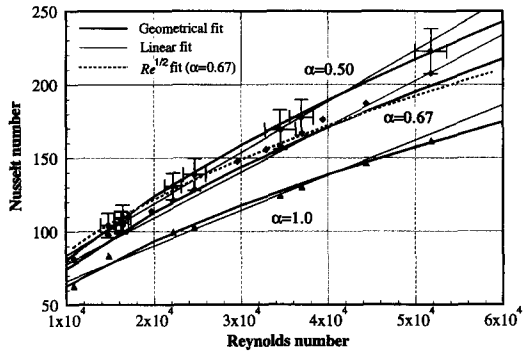

Fig. 9. The overall Nusselt number $\overline{Nu}$ of particles with axial ratios of 0.5, 0.67 and 1.0, rotating about a horizontal axis, as function of Re; with geometric (thick lines), linear (thin lines) and $Re^{1/2}$ (dashed line) fits. Note that $\overline{Nu}$ is affected neither by the rotation rate nor the configuration of the rotation axis.

spheroids, as described by $\overline{Nu}$ and $\overline{Sh}$. The Sherwood number, Sh, represents the dimensionless convective mass transfer coefficient. If it is assumed that the heat and mass transfer processes from a spheroid are similar, i.e. $\overline{Nu}$ and $\overline{Sh}$ have the same functional dependence of Re, and $\overline{Nu}$ can be used to express $\overline{Sh}$ by multiplying with a constant $(Pr/Sc)^{1/3}$ (≈ 1.046), for atmospheric conditions. Figure 10 gives $\overline{Nu}$ of spheroids obtained by several investigators.

Skelland and Cornish [13] conducted mass transfer experiments for the dissolution of non-rotating oblate naphthalene spheroids with $\alpha = 0.33$–1.0. They were able to describe the data for all spheroids with

$$\overline{Sh} = 0.74 Sc^{1/3} Re^{*1/2} \quad 200 < Re^* < 6000 \qquad (11)$$

where * indicates that the characteristic length was obtained by dividing the total surface area of the particle with its equatorial perimeter. This produces an implicit dependence on α of the form

$$\overline{Nu} \propto Re^{*1/2} \propto \sqrt{(f(\alpha))}\, Re^{1/2} \qquad (12)$$

where

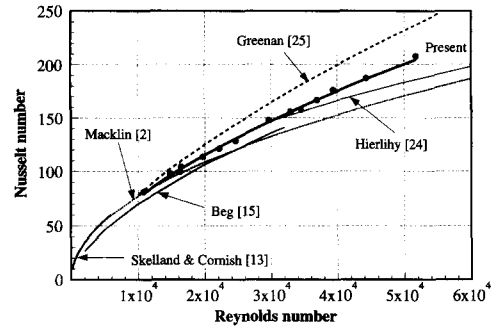

Fig. 10. Comparison of the overall Nusselt number $\overline{Nu}$ from spheroids ($\alpha = 0.67$) with the data on mass transfer by Beg [15], Skelland and Cornish [13], Macklin [2] and Hierlihy [24], and on heat and mass transfer by Greenan [25]. Greenan's data includes effect of surface roughness. The Reynolds number used in this figure is based on the maximum dimension of the particle. With the exception of Greenan's work all the others worked with non-rotating spheroids.

$$f(\alpha) = \frac{1}{2} + \frac{1}{4}\left(\frac{\alpha^2}{\sqrt{(1-\alpha^2)}}\right) \ln \frac{1+\sqrt{(1-\alpha^2)}}{1-\sqrt{(1-\alpha^2)}}$$

$$\alpha < 1.0. \qquad (13)$$

Hierlihy [24] measured the overall mass transfer of a non-rotating sphere and five non-rotating oblate spheroids with $\alpha = 0.33$–1.0, for the Re^* range of $3 \times 10^4 < Re^* < 4 \times 10^5$. Using an electrochemical method, he obtained, for flow parallel to the minor axis,

$$\overline{Sh} = 1.51 Sc^{1/3} Re^{*0.43} \propto f(\alpha)^{0.43} Sc^{1.3} Re^{0.43} \qquad (14)$$

where the power factor of Re is less than 1/2.

Beg [15] investigated the overall mass transfer from stationary naphthalene spheroids with $\alpha = 0.25$–1.0 over the range of $2 \times 10^3 < Re^* < 3.2 \times 10^4$. He proposed mass transfer coefficients given by

$$\overline{Sh} = 0.26 Sc^{1/3} Re^{*0.6} \propto f(\alpha)^{0.6} Sc^{1/3} Re^{0.6}. \qquad (15)$$

By measuring the melting rates of the non-rotating, spheroidal ice particles, Macklin [2] found that more heat and mass was transferred from spheroidal particles than from spherical particles with the same diameter. After relating the $\overline{Nu}$ results to Ranz and Marshall's formulations for spheres, he proposed the following shape factor χ as affected by α

$$\chi = 1.699 - 0.432\alpha. \qquad (16)$$

χ is defined as the ratio of heat transfer from a spheroid to that of a sphere with the same diameter as predicted by Ranz and Marshall [12]. It is apparent that the heat transfer of spheroids depends heavily on α.

As seen in Fig. 10, $\overline{Nu}$ from this study are higher than those of Macklin ($\alpha = 0.67$ [2]) and smaller than those of Greenan ($\alpha = 0.62$–0.69 [25]) whose arti-

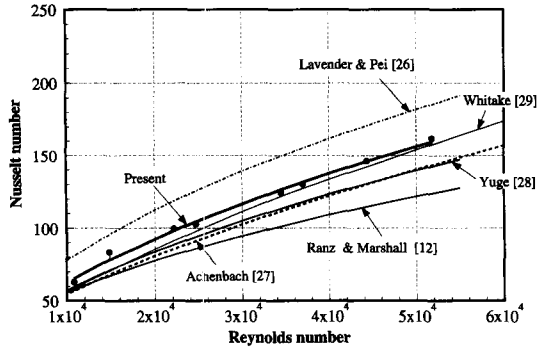

Fig. 11. Comparison of the overall Nusselt number $\overline{Nu}$ from rotating spheres with non-rotating particles as obtained by Lavender and Pei [26], Achenbach [27], Whitaker [29], Ranz and Marshall [12] and Yuge [28].

ficially grown gyrating ice particles had a certain roughness which would enhance the convective heat transfer. Figure 10 also shows $\overline{Nu}$ of spheroids with $\alpha = 0.67$, given by Beg [15], Hierlihy [24], and Skelland and Cornish [13]. The Reynolds numbers used in Fig. 10 were all reduced to the major axis diameters for $\alpha = 0.67$. $\overline{Nu}$ of Beg is smaller than that of this study, whereas Skelland and Cornish give $\overline{Nu}$ close to it.

Another comparison is given for $\overline{Nu}$ of non-rotating spherical particles (Fig. 11). The present results are smaller than those of Lavender and Pei [26] and higher than those of Achenbach [27] and Yuge [28]. However, $\overline{Nu}$ values in this study are close to those by Whitaker [29], who summarized many proposed relations. They are significantly larger than those predicted by the expanded Ranz and Marshall formulation [12]; further, the value of the power term of Re is larger than 0.5 commonly assumed. $\overline{Nu}$ values by Whitaker are ~25% larger than those of Ranz and Marshall, and 30% higher than in the present investigation. This difference is important because $\overline{Nu}$ commonly used in the existing hail studies is extrapolated from Ranz and Marshall's work. An increase in Nusselt number will delay the onset of wet growth and shedding of raindrops from hailstones. Both effects limit hail growth and, therefore, will lead to larger hailstones in hailstorms.

SUMMARY AND CONCLUSIONS

A method was developed to measure and assess the latitudinal and overall convective heat transfer from rotating spheres and spheroids with limited heat conductivity and, thus, non-uniform surface temperatures. It is based on local surface temperature measurements of particles cooling in a wind tunnel with an infrared imaging system. At the same time, a numerical technique was used to calculate the time evolution of the internal temperature distribution, the heat conduction within the particle, the surface heat flux, and the latitudinal and overall convective heat transfer coefficients. The following conclusions were drawn from the experiments and related calculations covering a Reynolds number range of $1.1 \times 10^4 < Re < 5.2 \times 10^4$.

(1) A self-consistent method was developed to physically solve in a consistent fashion heat transfer problems in a moving fluid for fixed or rotating particles with limited thermal conductivities. This method is necessary to examine more complex heat transfer processes involving phase changes, chemical reactions, accretion or deposition of other particles not in thermal equilibrium, radiation, etc. which cannot be added to overall or averaged heat transfer processes without severe distortions.

(2) The latitudinal convective heat transfer of rotating spheres and spheroids has been established. The latitudinal variation is 25–45% of the overall value for rotating particles with the minor (rotational) axis perpendicular to the airflow and over 100% for the particles with the minor axis parallel to the airflow. At an air temperature of -15°C and an initial model temperature of -6°C, the maximum difference between polar and equatorial temperatures was up to 3°C.

(3) An overall Nusselt number, $\overline{Nu}$ was defined for spheroidal particles and calculated by integrating the latitudinal transfers over the surface. It is dependent on Reynolds number and the spheroidicity of the particle. The relationships between $\overline{Nu}$ and Re are given by equations (9) and (10). The power factor of Re in expression (9) is larger than 0.5 and increases with decreasing α. $\overline{Nu}$ for spheroids with $\alpha \leqslant 0.67$ are up to 40% higher than for spheres with the same diameter.

(4) Although the position of the rotation axis causes different latitudinal variations of heat transfer, it has no effect, within the error bars of the experiments, on the total transfer as integrated over latitude. The same is true for rotation rates of $5 \leqslant f_1 \leqslant 22$ Hz, corresponding to Strouhal numbers $0.005 \leqslant Sr \leqslant 0.06$.

(5) Non-rotating and rotating ($f_1 \leqslant 22$ Hz) particles have, within the experimental error, the same overall heat transfer coefficients.

(6) $\overline{Nu}$ for a spherical particle ($\alpha = 1.0$) is approximately 30% larger than that predicted by Ranz and Marshall and commonly used in hail studies.

(7) Comparisons of $\overline{Nu}$ for spheres and spheroids (mostly non-rotating) with the overall values measured directly by other authors are in good agreement with the present data, which depend on the integration over latitudinal heat transfer coefficients.

While the results simulate solutions for materials of specific thermal diffusivities, the surface temperature variations of spheres and spheroids would be different for other diffusivities, and the true convective heat transfer would have to be modeled afresh for different basic particle materials. However, comparison with the literature suggests that thermal diffusivities

changes of materials like copper and ice or maybe beyond, do not affect the overall heat transfer.

Acknowledgements—This work was sponsored by the Natural Sciences and Engineering Research Council of Canada (NSERC). Special thanks go to the Ontario Lightwave and Laser Research Centre (OLLRC) for making the AGEMA system available. Without it, this study would not have been possible. One author (GZ) is grateful to the University of Toronto for providing a Connaught Scholarship and the Chinese Government for financial support.

REFERENCES

1. R. List, Kennzeichen atmospharischer Eispartikeln, 2. Teil, *Z. Angew. Math. Phys.* **9a** 217–234 (1958).
2. W. C. Macklin, Heat transfer from hailstones, *Quart. J. Meteor. Soc.* **89,** 360–369 (1963).
3. W. C. Macklin, The characteristics of natural hailstones and their interpretation. In *Hail: A Review of Hail Science and Hail Suppression,* Meteorological Monograph No. 16, American Meterological Society, Boston, MA, pp. 65–88 (1977).
4. B. L. Barge and G. A. Isaac, The shape of Alberta hailstones, *J. Rech. Atoms.* **7,** 11–20 (1973).
5. R. J. Matson and A. W. Huggins, The direct measurement of the sizes, shapes, and kinematics of falling hailstones, *J. Atmos. Sci.* **37,** 1107–1125 (1980).
6. C. A. Knight and N. C. Knight, The falling behavior of hailstones, *J. Atmos. Sci.* **27,** 672–681 (1970).
7. R. List, G. B. Lesins, F. García-García and D. B. McDonald, Pressurized icing tunnel for graupel, hail and secondary raindrop production, *J. Atmos. Oceanic Technol.* **4,** 454–463 (1987).
8. T. E. W. Schumann, The theory of hailstone formation, *Quart. J. R. Meteor. Soc.* **64,** 3–21 (1938).
9. F. H. Ludlam, The composition of coagulation-elements in cumulonimbus, *Quart. J. R. Meteor. Soc.* **76,** 52–58 (1950).
10. R. List, Wachstum von Eis-Wassergemischen im Hagelversuchskanal, *Helv. Phys. Acta.* **32,** 293–296 (1959).
11. R. List and J. G. Dussault, Quasi steady state icing and melting conditions and heat and mass transfer of spherical and spheroidal hailstones, *J. Atmos. Sci.* **24,** 522–529 (1967).
12. W. E. Ranz and W. R. Marshall, Evaporation from drops I & II, *Chem. Engng Prog.* **48,** 141–146, 173–180 (1952).
13. A. H. P. Skelland and A. R. H. Cornish, Mass transfer from spheroids to an air stream, *A.I.Ch.E. Jl* **9,** 73–76 (1963).
14. J. H. Masiliyah and N. Epstein, Numerical study of steady flow past spheroids, *J. Fluid Mech.* **44,** 493–512 (1970).
15. S. A. Beg, Forced convective mass transfer studies from spheroids, *Wärme-und-Stoffübertragung* **8,** 127–135 (1975).
16. G. G. Zheng, An experimental investigation of convective heat transfer of rotating and gyrating hailstone models, Ph.D. Thesis, University of Toronto (1994).
17. P. V. Hobbs, *Ice Physics.* Oxford University Press, Oxford (1974).
18. M. N. Ozisik, *Heat Conduction* (2nd Edn). John Wiley, New York (1993).
19. G. E. Myers, *Analytical Methods in Conduction Heat Transfer.* McGraw-Hill, New York (1971).
20. G. G. Zheng and R. List, Measurements of convective heat transfer of hailstone models, *Proceedings 11th International Conference on Cloud and Precipitation,* 17–22 Aug., Montreal, pp. 44–47 (1992).
21. F. P. Incropera and D. P. DeWitt, *Fundamentals of Heat and Mass Transfer* (3rd Edn). John Wiley, Toronto (1990).
22. W. M. Kays and M. E. Crawford, *Convective Heat and Mass Transfer* (3rd Edn). McGraw-Hill, New York (1993).
23. L. C. Thomas, *Heat Transfer.* Prentice Hall, New Jersey (1993).
24. R. D. Hierlihy, Measurements of the mass transfer of spheroidal hailstones, M.Sc. Thesis, University of Toronto (1968).
25. B. J. W. Greenan, Hailstone heat and mass transfer measurements, Ph.D. Thesis, University of Toronto (1993).
26. W. J. Lavender and D. C. T. Pei, The effect of fluid turbulence on the rate of heat transfer from spheres, *Int. J. Heat Mass Transfer* **10,** 529–539 (1967).
27. E. Achenbach, Heat transfer from spheres up to $Re = 6 \times 10^6$, *Int. J. Heat Mass Transfer* **113,** 199–207 (1991).
28. T. Yuge, Experiments on heat transfer from spheres including combined natural and forced convection, *Int. J. Heat Mass Transfer* **82,** 214–220 (1960).
29. S. Whitaker, Forced convection heat transfer correlations for flow in pipes, past flat plates, single cylinders, single spheres, and for flow in packed beds and tube bundles. *A.I.Ch.E. Jl* **18,** 361 (1972).